LA-UR-23-27355

Approved for public release; distribution is unlimited.

Title:	Modeling a Miniature Voitenko-Like Explosively-Driven Shock Tube Using FLAG
Author(s):	Holmes, Matthew Cradin
Intended for:	Report
Issued:	2024-01-11 (rev.1)

Modeling a Miniature Voitenko–Like Explosively–Driven Shock Tube Using FLAG

Matthew C. Holmes

LA-UR-24-XXXXX
January 7, 2024

Prepared for: U.S. Department of Energy/National Nuclear Security Administration
Los Alamos Field Office
Carl E. Johnson
Scientist
XTD-PRI

Prepared by: Matthew C. Holmes
Post-Masters Intern
XCP-8

Contents

Figures

Contents

Tables

Executive Summary

Hypervelocity launcher technology enables experimental study of hypervelocity impacts like those that occur in orbital collisions. Such devices often involve the acceleration of gases to velocities on the order of km/s. However, it is challenging to accurately numerically model the acceleration of gases through simple cylindrical shock tubes, and such a numerical capability is a prerequisite to the accurate simulation of gases accelerating through more complex geometries or within functioning hypervelocity launchers.

In particular, simulation of explosively–driven shock tubes is difficult because the jet velocity is sensitive to a number of parameters including gas densities and pressures, shock tube diameter, material used for the rupture membrane and its thickness, as well as HE performance properties [1]. Here, we describe models produced using the Free–Lagrange (FLAG) hydrocode [2–6], which is developed and maintained by the Los Alamos National Laboratory (LANL).

Using FLAG's 2D cylindrical geometry we simulate hypervelocity jets observed in a miniature explosively–driven shock tube experiment [7]. The experiment used a device based on the Voitenko accelerator design [8] and consisted of a pellet of high explosive driving a piston into a gas compression chamber. A membrane ruptures sending compressed gas into a shock tube. This report presents characteristic models in which FLAG produces turbulent jets.

We present a simulation in which FLAG simulated a total of 5.00 μs beginning with detonation of the PBX–9407 at $t = 0$. The steel piston achieved a velocity of ~ 4.955 km/s before reaching the bottom of the compression chamber. After puncture of the membrane the compressed air quickly expanded into the shock tube, accelerating away from the steel material. The jet traveled at 14.88 ± 0.097 km/s (95% confidence interval) between 4.12 μs and 5.00 μs simulation time. Taking the velocity 15.99 km/s observed in experiment [7] as truth the simulated velocity had a relative error of 6.94%. Encouragingly, both a simple analytic model for shock tube escape velocity and the numerical model computed using FLAG predict jet velocities within 1.11 km/s of the observed experimental jet velocity.

We also discuss results of models that use a fixed kinetic boundary condition in place of a physical membrane, the effect of compressing helium instead of air on jet velocity, the results of a mesh convergence study, and an alternative metric for jet velocity. Overall, the results show that FLAG can produce models of hypervelocity jet acceleration that are fairly consistent with observations and that may be adequate for certain applications or for incorporation with simulations of larger systems, but that more work is required to robustly simulate such phenomena and for simulations to be used for prediction.

Acknowledgements

Area of Contribution	Contributor	Affiliation
HE Modeling	Stephen Andrews	XCP-8
Mentorship	Joanne Budzien	XCP-8
FLAG Support	Miles Buechler	XCP-1
Mentorship	Wendy Caldwell	XCP-8
FLAG Support	Nick Denissen	XTD-PRI
Mentorship and Project Leadership	Carl Johnson	XTD-PRI
FLAG Support	Mack Kenamond	XCP-1

This work was supported by the Advanced Simulation and Computing (ASC)– Verification and Validation (V&V) program at LANL. Los Alamos National Laboratory, an affirmative action/equal opportunity employer, is operated by Triad National Security, LLC, for the National Nuclear Security Administration of the U.S. Department of Energy under contract 89233218NCA000001.

1 Introduction

Interest in hypervelocity impacts involving microparticles is growing in part because of the threat of micrometeorite impacts to the rapidly increasing human presence in low earth orbit. Current experimental techniques used to study impacts are limited in their maximum velocities. For example, the National Aeronautics and Space Administration's two stage light–gas guns can accelerate particles to ~ 8.4 km/s [9]. However, micrometeorites typically travel at velocities on the order of 10 km/s [10] and the average relative velocity of orbital collisions has been calculated to be ~ 10 km/s [11]. Hypervelocity impact experiments are also important in material science when developing armor. For example, a newly created nano–architected material [12] is able to stop particles traveling at supersonic speeds more effectively than Kevlar.

Improving experimental capabilities for hypervelocity impact can advance our understanding of the hazards involved in orbital collisions and provide better testing of the mechanical limits of newly developed materials used for armor against projectiles. Shock tube devices may enable impact experiments at higher velocities. Recently, an explosively–driven light–gas gun [13] was demonstrated to be capable of launching 8 mm diameter impactors to velocities greater than 10 km/s: a notable advance in hypervelocity launcher technology.

Design of explosively–driven hypervelocity launchers is challenging as is successful imaging of the impact. The initial location of a particle must not be so close to the high explosive (HE) that it will vaporize and not so close to the target that it will fail to reach the desired velocity. Numerical simulation can guide experimental design by predicting locations that particles should be placed in order to achieve a certain velocity before impact. Simulation can also provide insight into how long after detonation of the HE an impact will occur.

The experiment described by Johnson et al. [7] consists of a ~ 13 mm diameter right cylindrical pellet of polymer–bonded high explosive 9407 (PBX–9407) driving a stainless steel piston into a gas compression chamber, which is separated from the sub–millimeter diameter shock tube by a thin (~ 25 μm) mica membrane. The membrane eventually ruptures and the compressed gas is released into the evacuated shock tube creating a hypervelocity jet. Two of these miniature shock tube devices are shown in Figure 1-1 and additional dimensions of the device can be found in Ref. [7].

Design of the miniature shock tube was informed by ALE3D [14] hydrocode modeling performed at the Lawrence Livermore National Laboratory. However, ALE3D simulations resulted in an average jet velocity of ~ 10 km/s, while the experimental jet velocity was measured to be ~ 16 km/s [1]. Accurately modeling the acceleration of gas through a tube is generally a difficult problem. Here, we describe our FLAG simulation that achieved a jet velocity of ~ 15 km/s with a 7% relative error.

Introduction

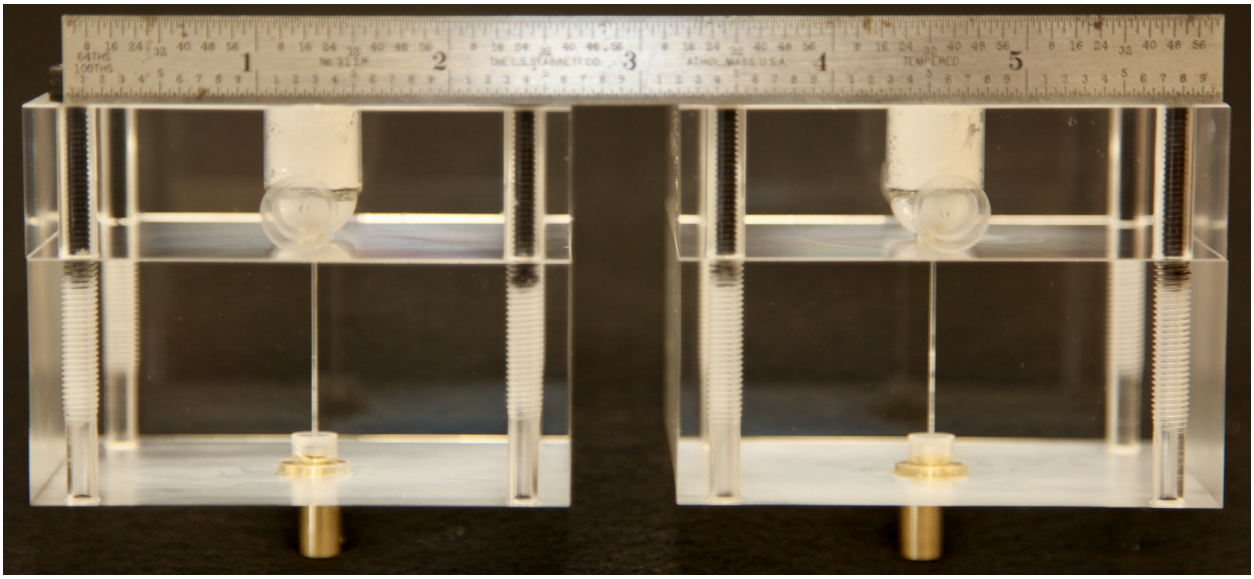

Figure 1-1: Two miniature high explosive–driven shock tube devices used in the experiments described by Johnson et al. [7].

2 Methods

To model the miniature shock tube device described by Johnson et al. [7] we used the FLAG hydrocode introduced in Sec. 1. FLAG is a massively parallel finite–volume arbitrary Lagrangian–Eulerian code [15] that supports adaptive mesh refinement (AMR) as well as various constitutive models [5], which allow for solid materials to be modeled. FLAG accesses LANL's Simulation-Enabled Safeguards Assessment Methodology (SESAME) database for tabular equation of state (EOS) data [16]. FLAG also includes robust high explosive modeling routines including various detonation, burn, and EOS models [5]. The model geometry (Fig. 2-1), meshing strategy, and material models are discussed in what follows.

2.1 Computational Mesh and Geometry

We chose to run FLAG using a completely Eulerian mesh relaxer in order to avoid mesh tangling often caused by high vorticity and turbulent dynamics, which we expected in the system. An estimation of the Reynolds number describing the high velocity jet produced in experiment can be given by

$$\mathrm{Re} = \frac{\rho u D}{\mu} = 6.92 \times 10^5, \tag{1}$$

using values of $\rho = 1.23$ kg/m^3 and $\mu = 18.2 \times 10^{-6}$ kg/(m s) for density and dynamic viscosity [17] of air at standard temperature and pressure, $u = 16.0 \times 10^3$ m/s for jet velocity, and $D = 6.40 \times 10^{-4}$ m for the inner diameter of the shock tube. Such a Reynolds number indicates turbulent flow because it is far larger than the critical value $\mathrm{Re} = 2.30 \times 10^3$ [18, 19].

We took advantage of FLAG's AMR capability to prioritize resolution of material boundaries, as well as regions determined during run–time using three different methods: exceeding a user-defined pressure difference threshold for any two adjacent zones triggered refinement, specific energy in the HE material triggered refinement based on an error distribution–based approach described by Bo and Shashkov [20], and exceeding a pressure threshold in zones containing air triggered refinement in those zones. Because the miniature shock tube device has a high degree of axial symmetry about the tube we modeled the system in FLAG's 2D cylindrical geometry in which azimuthal symmetry is assumed.

Figure 2-1 shows the geometry at the start of simulation colored by density and refinement level with the components labeled. The coarsest mesh had a zone size of $dx = 101.6$ μm (light grey regions in Fig. 2-1), while the most finely resolved mesh was used only for initial refinement of the compression chamber and the membrane and for refinement of the membrane boundary during simulation and used $dx = 3.175$ μm (dark purple regions in Fig. 2-1). All other refined features used an intermediate resolution of $dx = 12.70$ μm. FLAG's simulation timestep is adaptive and ranged between 1 picosecond and 1 nanosecond with the largest timesteps during the HE burn and the smallest timesteps during rupture of the membrane, which was resolved more finely than any other feature in the model.

The compression chamber and brass insert regions were created using Hermite curves based on the original schematics of Johnson et al. [7] and were not conformal within the mesh. In other words, the boundaries of these regions passed through zones in the mesh creating multi-material zones, which were refined to approximate a smooth interface between materials. However, we did attempt to align the mesh with material boundaries whenever possible in order to maximize

Methods

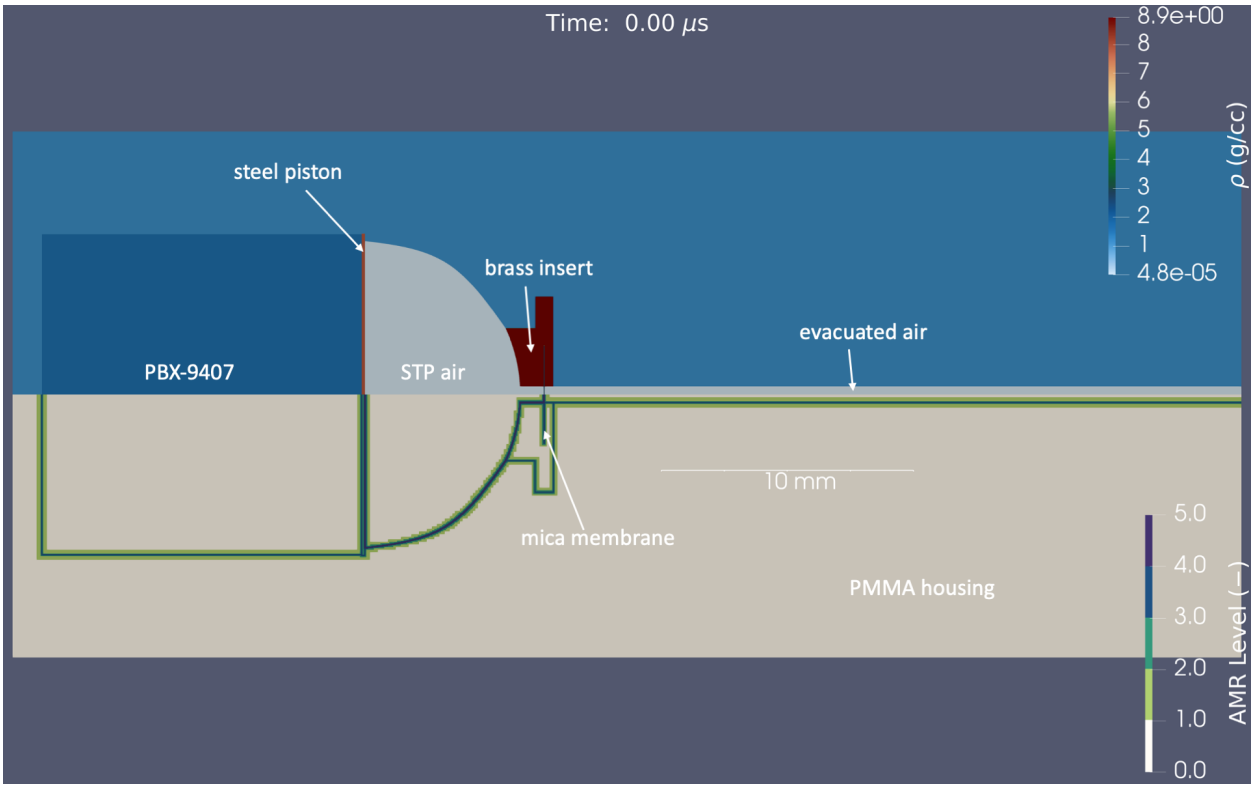

Figure 2-1: The computational domain at $t = 0$ colored by density (top) and refinement level (bottom) with each component labeled. Coloring by refinement levels helps expose the position and dimensions of the membrane and emphasizes the effect of using AMR.

hydrostatic equilibrium. For example, the shock tube had a diameter of 0.64 mm and its boundary was aligned with the edges of the mesh. The edges of the PBX-9407 and the steel piston were also aligned with the mesh. Clamped within the brass insert was the mica membrane, which had a diameter of 3.874 mm and thickness of 25.40 μm.

Using a 2D geometry the gas fitting and connector tube (shown in Fig. 1-1) that was used to allow gas flow in the compression chamber could not be modeled realistically. We thought this to be a reasonable omission because only a small percentage of the total gas should flow from the chamber into the connector tube before the membrane ruptured. This is because the piston was expected to have a high velocity (on the order of km/s) and the volume of the compression chamber was much larger than that of the connector tube (e.g., the shock tube had 7.6% the volume of the compression chamber). Therefore, pressure would increase within the connector tube much more rapidly than in the chamber, causing the majority of the gas to flow downstream toward the membrane. We decided that, if warranted, we would include the gas fitting and tube in a 3D model.

We also omitted the gas fitting at the bottom of the device used to create vacuum conditions in the shock tube because we were not interested in the jet's interaction with material at the end of the shock tube; we were primarily focused on accurately modeling the jet velocity as it traveled down the tube.

Finally, the housing was modeled as one piece instead of two because including this detail would introduce more zones in the mesh and would be practically indistinguishable within the model.

2.2 Material Models

The model geometry contained seven distinct regions composed of six different materials: air, copper, mica, PBX–9407, polymethyl methacrylate (PMMA), and stainless steel 304 (SS–304). Copper was used to model the brass insert in the absence of a suitable brass model. Table 2-1 summarizes the EOS, strength, and failure models used. We initialized all materials at standard temperature-pressure[1] (STP) except the air in the evacuated shock tube, which was initialized at 40 mbar in accordance with the experiment by Johnson et al. [7]. We note that FLAG's iterative initialization routine provided the STP air with a density of 1.23 mg/cc and the near vacuum air with a density of 47.9 μg/cc.

Our copper and steel materials employ the Preston–Tonks–Wallace (PTW) [21, 22] viscoplasticity strength model, while our PMMA uses FLAG's isotropic elastic/plastic response model with shear modulus, yield strength, and melt temperature parameters from Steinberg [23]. Although highly anisotropic, our mica was given the isotropic strength model as a first approximation.

[1] We define STP as 293.15 K and 1 atm.

Table 2-1: Equation of state, strength model, and failure model for each material in the system.

Material	EOS	Strength	Failure
Air	SESAME	–	–
Copper	SESAME	PTW	P_{min}/η_{min} Spall
Mica	SESAME	Isotropic Elastic/Plastic	P_{min}/η_{min} Spall
PBX–9407	JWL	–	–
PMMA	SESAME	Isotropic Elastic/Plastic	P_{min}/η_{min} Spall
SS–304	SESAME	PTW	P_{min}/η_{min} Spall

Methods

We also use a basic failure model in which a material fails once the tensile pressure exceeds a given value or the compression falls below a given value. Both strength and failure parameters used in the mica model come from S&R Optic GmbH [24], which provides a range of values for shear modulus (220-260 MPa), compressive strength (190-280 MPa), and melt temperature (970-1300 K). The model presented here uses the minimums of these values. We found no significant change in jet velocity when the maximum values were used.

The PBX–9407 material uses the Lund programmed burn model [25, 26] together with the Jones–Wilkins–Lee (JWL) EOS [27] with parameters from Dobratz [28]. These parameters resulted in the PBX-9407 being initialized with Chapman-Jouguet (CJ) pressure $P_{CJ} = 2.6$ GPa and detonation velocity $D_{CJ} = 7.7$ km/s. To achieve planar detonation waves we initialized the HE with 50 point detonators along its top boundary.

The air material model was used for both the STP air in the compression chamber and the near vacuum air in the shock tube. In the early stages of model development we observed an issue with the air material that was causing a timestep crash during jet flow. Specifically, the near vacuum air material used SESAME table 5030, which is often troublesome because it does not have a zero temperature isotherm. Initializing the air at low density (47.9 μg/cc) exacerbated the problem.

One solution was to switch to helium, but because jet velocity is proportional to the sound speed of the gas at maximum compression, using helium was expected to produce higher shock speeds than air [29]. Therefore, to avoid the timestep crash we used a developmental air EOS (table 5031) that includes the zero temperature isotherm.

3 Results

FLAG simulated a total of 5.00 μs beginning with detonation of the PBX–9407 at $t = 0$. This was long enough for the piston to compress the air in the hemispherical chamber, the mica membrane to rupture, and the jet to traverse the entire length of the shock tube (Fig. 3-1). The steel piston achieved a velocity of ~ 4.955 km/s before reaching the bottom of the compression chamber. The mica membrane did not rupture until the steel piston struck the brass insert, deformed, and punctured the membrane. After puncture of the membrane the compressed air quickly expanded into the shock tube, accelerating away from the steel material.

Figure 3-1 shows the compressed air jetting down the shock tube and should be compared with frames 11–15 of Fig. 2 in the report by Johnson et al. [7]. It is observed that after the highly compressed gas is released within the tube it accelerates to a greater velocity than that of the shock propagating through the PMMA housing.

During the experiment Johnson et al. [7] recorded the apparent jet position every 225 ns for 900 ns to obtain five data points. A line was fit to these five points with slope representing average jet velocity. The jet was observed to move from a position of ~ 10.1 mm to ~ 24.5 mm with a jet velocity of 15.99 ± 0.54 km/s (95% confidence interval).

In Fig. 3-2 we plot jet position data from our simulation (back points), measuring jet position as the point furthest downstream from the membrane with particle velocity greater than 3.000 km/s in the axial direction (parallel to the tube walls). We compute three linear fits of the data over three time intervals to estimate jet velocity.

Fit y_1 shows that for 319 ns immediately after membrane rupture the jet had a velocity of 20.65 km/s and y_2 shows that the jet decelerated to a velocity of approximately 14.21 km/s. Fit y_3 shows that the jet traveled at 14.88 ± 0.097 km/s (95% confidence interval) between 4.12 μs and 5.00 μs simulation time: a time interval comparable to that used by Johnson et al. [7] for collection of experimental data. Taking 15.99 km/s as truth the velocities estimated using fits y_1, y_2, and y_3 have relative errors of 22.7%, 11.1%, and 6.94% respectively.

Theoretically, the escape velocity in a classical shock tube is given by

$$U = \frac{2C_0}{\gamma - 1}, \tag{2}$$

where U is escape velocity, C_0 is sound speed of the compressed gas, and γ is its ratio of specific heats [29]. In our model, the volume averaged pressure and sound speed observed in the compressed gas just before membrane rupture was 2.49 GPa and 3.32 km/s, respectively. Assuming an ideal EOS and taking $\gamma = 1.40$, the above formula predicts an escape velocity of 16.60 km/s, which has a 3.82% error compared to the experimental value 15.99 km/s. Encouragingly, both the analytic model for shock tube escape velocity and the numerical model computed using FLAG predict jet velocities within 1.11 km/s of the observed experimental jet velocity.

However, we note that by $t = 4.18$ μs a small mass (on the order of μg) of steel traveling along the PMMA boundary of the shock tube surpassed the front of the jet. By $t = 4.50$ μs a second mass of steel traveling along the axisymmetric boundary of the computational domain (and the axial center of the shock tube) surpassed the first mass of steel. These two masses can be seen in the bottom panel of Fig. 3-3 and are responsible for the acceleration of the jet to 14.88 km/s observed in Fig. 3-2. Without this effect the jet velocity would have been measured to be smaller.

Results

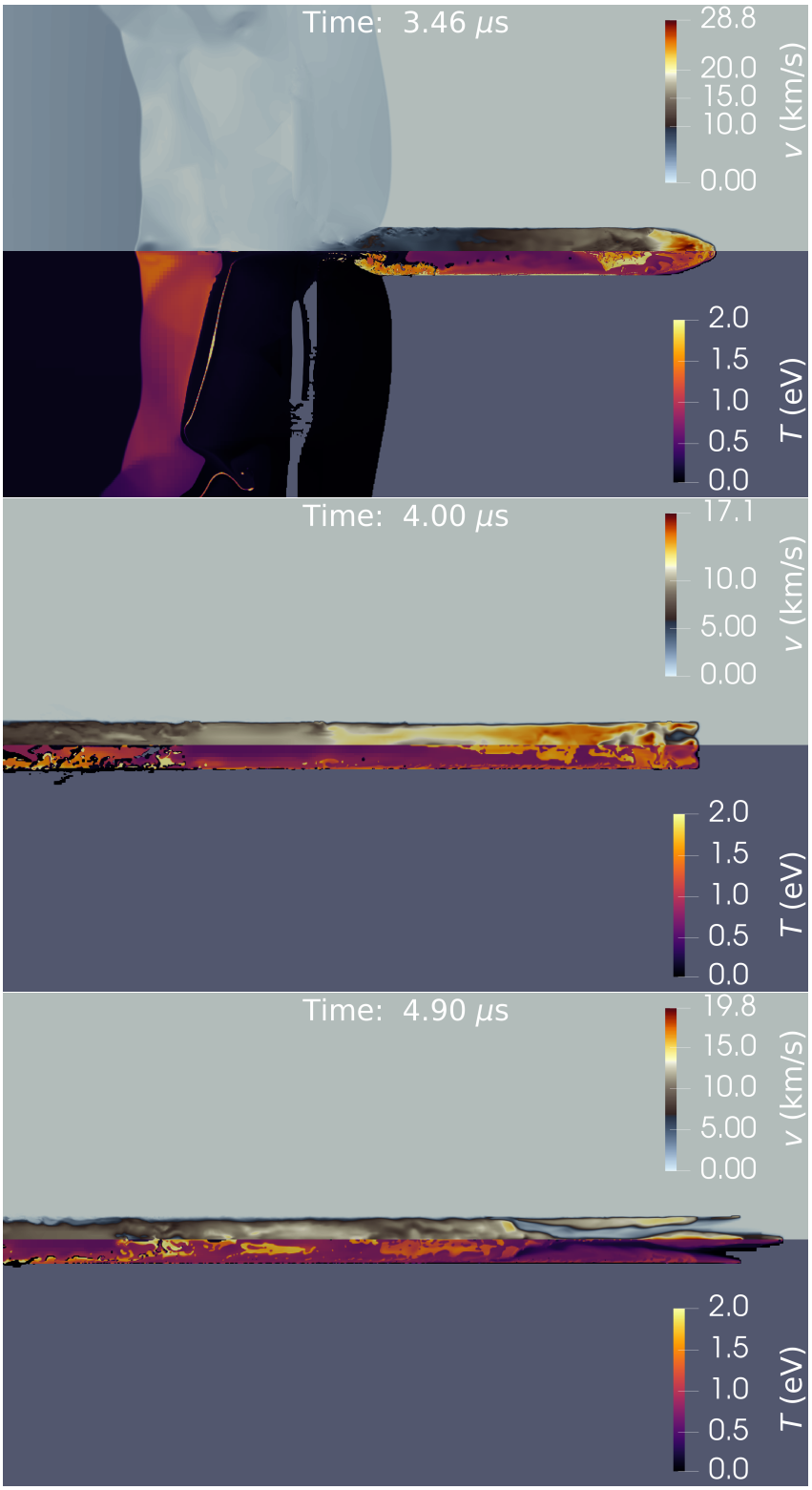

Figure 3-1: A series of visualizations of the FLAG simulation colored by velocity (top of each panel) and temperature (bottom of each panel) showing the jet flow down the shock tube.

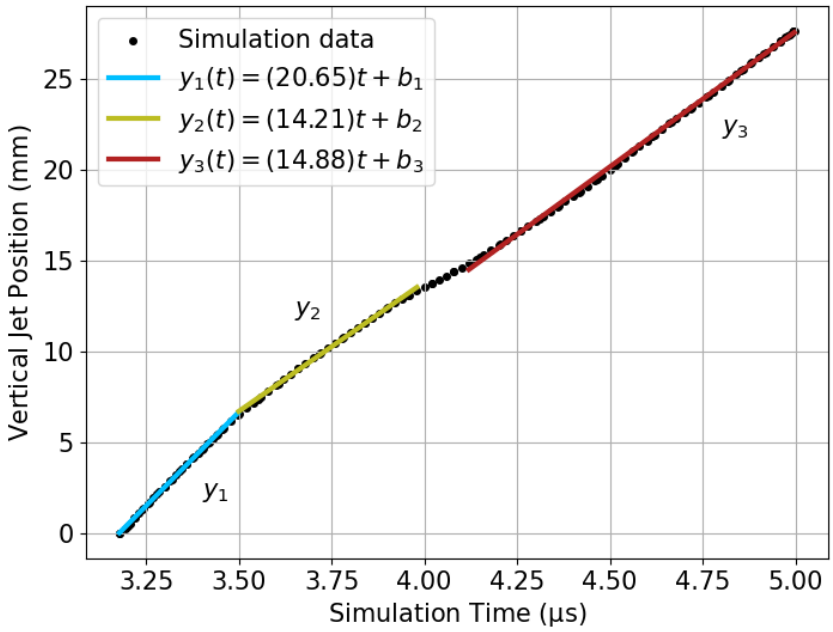

Figure 3-2: Vertical jet position (black points) with least squares linear fits y_i plotted as functions of time. Fits 1, 2, and 3 are computed over time intervals $[3.18, 3.50]$, $[3.50, 3.98]$, and $[4.12, 5.00]$ μs respectively.

Results

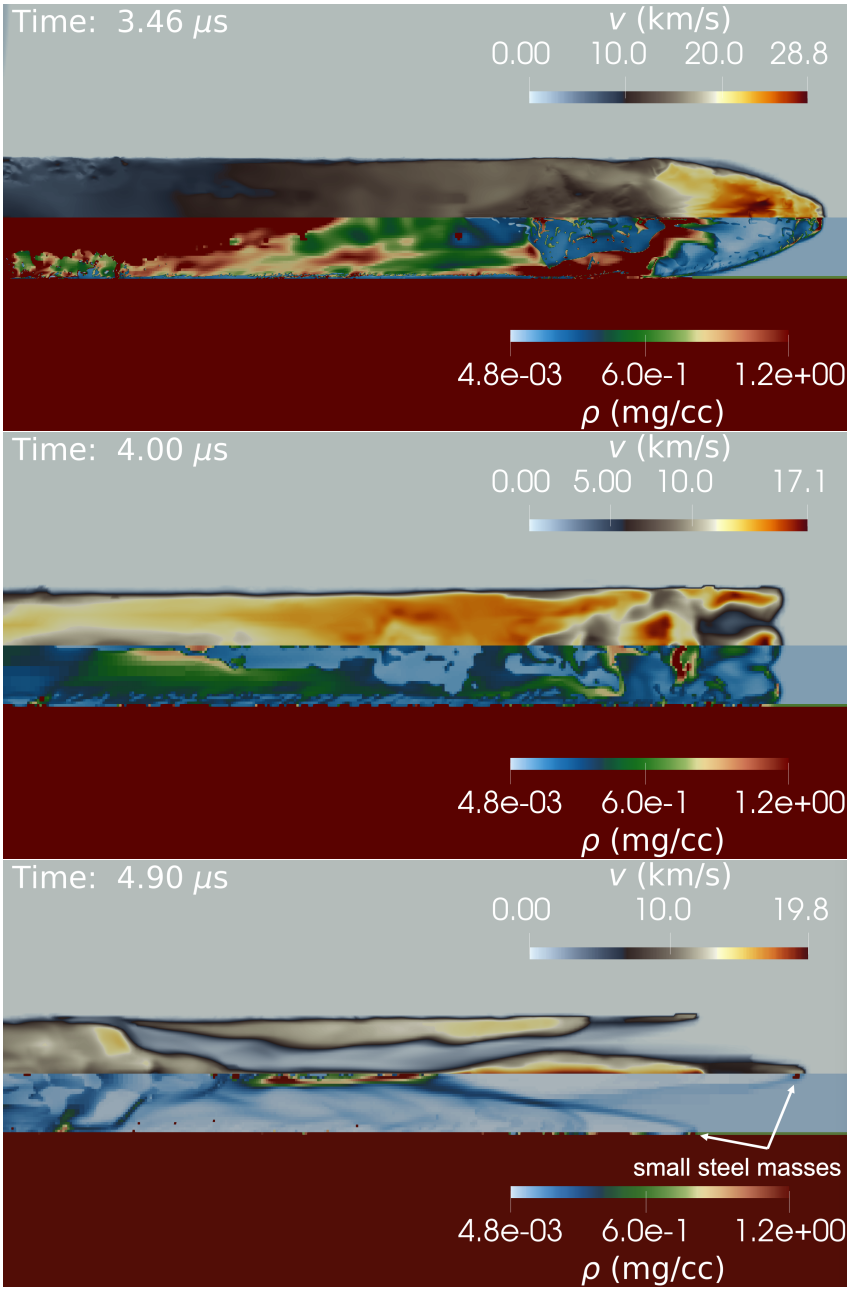

Figure 3-3: A series of visualizations of the FLAG simulation colored by velocity (top of each panel) and density (bottom of each panel) showing the jet flow down the shock tube.

3.1 Foregoing a Physical Membrane

To determine the role of the mica membrane in the development of the jet we ran an additional simulation that was identical to the first except that it did not use a physical membrane. Instead, the model used a fixed kinetic boundary condition (KBC) to "separate" the volumes of STP and low pressure until simulation time $t = 3.19$ μs, when the membrane was observed to rupture in the previous model.

The results of using a fixed KBC instead of a physical membrane are shown in Fig. 3-4. It is observed that the jet formed after release of the KBC is faster (on average over time) than the jet formed after rupture of the mica membrane. Also, Fig. 3-4 shows that at $t = 4.86$ μs the jet formed after release of the KBC remains relatively dense and is not led by small, dense masses of steel.

Figure 3-5 (upper left) shows the effect of using a KBC membrane on jet position over time. Because the shock tube length was ~ 27 mm the jet position does not exceed this value. According to the data of Fig. 3-5 the jet velocity decreased monotonically with time and had a larger average velocity than in the case of a mica membrane; the jet traveled further in a fixed period of time. However, as indicated by Fig. 3-5 (upper right) the jet was observed to have a velocity of 13.46 ± 0.060 km/s (95% confidence interval) over the time interval $[4.12, 4.84]$ μs, which has a relative error of 16% when compared to experiment.

On the other hand, Fig. 3-5 (lower center) shows that during the 880 ns interval $[3.44,\ 4.32]$ μs the jet had a velocity of 16.04 ± 0.22 km/s (95% confidence interval). This range of velocities lies completely within the 95% confidence interval of Johnson et al. [7] and has a relative error of 0.3%. However, this time interval was chosen specifically in order to minimize the relative error in jet velocity compared to experiment and we do not know exactly how this time interval compares to the 900 ns interval used to record experimental data.

Results

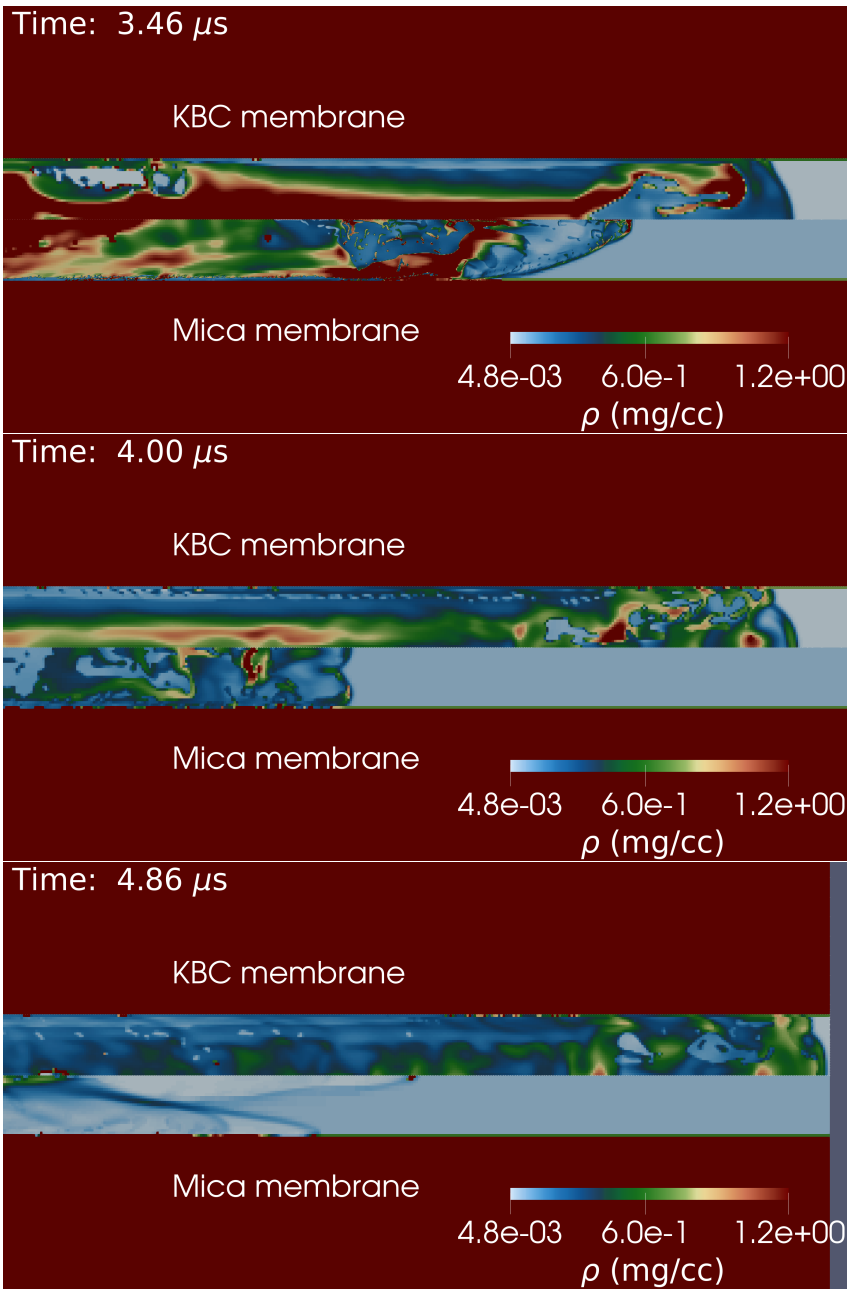

Figure 3-4: A series of visualizations of the FLAG simulation colored by density comparing the use of a fixed KBC membrane (top of each panel) with the use of a mica membrane (bottom of each panel).

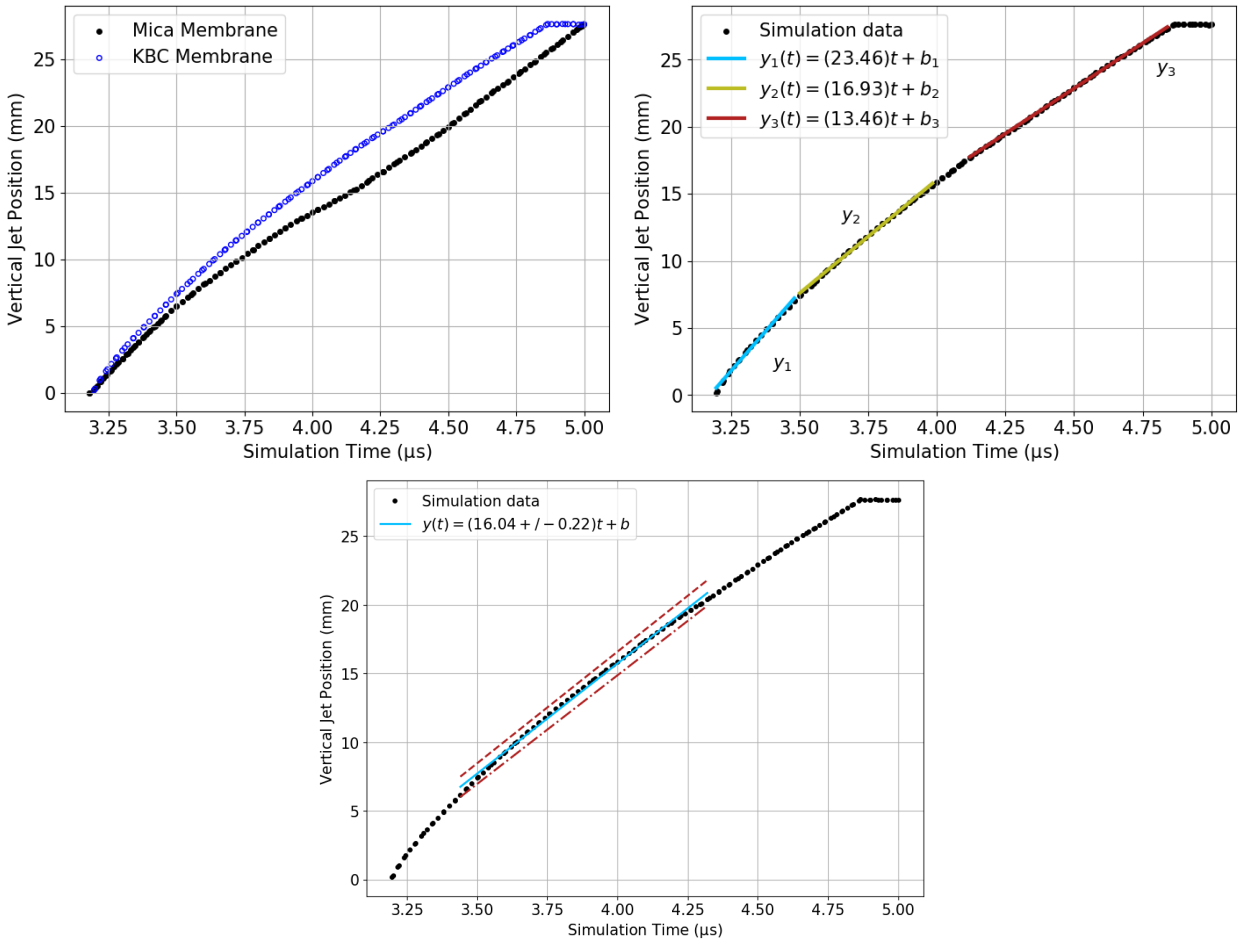

Figure 3-5: Vertical jet position in the case of a mica membrane (black points) compared to the case of a KBC (blue points) [upper left], jet velocity over time for the case of a KBC plotted in an analogous manner to Fig. 3-2 [upper right], and jet velocity over time for the case of a KBC with a linear fit (solid light blue) and its upper (dashed red) and lower (dash-dotted red) 95% confidence intervals [lower center].

3.2 Compressing Helium Versus Air

Here, we fill the compression chamber with STP helium instead of air. The helium was initialized at STP with a density of 0.166 mg/cc whereas the air had been initialized at STP with a density of 1.23 mg/cc. Computing the escape velocity using volume averaged sound speed just before rupture $C_0 = 14.01$ km/s from the FLAG simulation and $\gamma = 1.667$ for an ideal helium EOS we obtain

$$U = \frac{2C_0}{\gamma - 1} = 42.01 \text{ km/s}. \tag{3}$$

Figure 3-6 plots jet position and velocity versus simulation time. The model produced a jet with an average velocity of 36.61 ± 0.29 km/s. We note that the velocity obtained using helium appears more constant than the velocities obtained using air. For both gases, helium and air, FLAG produced jets with average velocities slower than those predicted by Eq. 3.

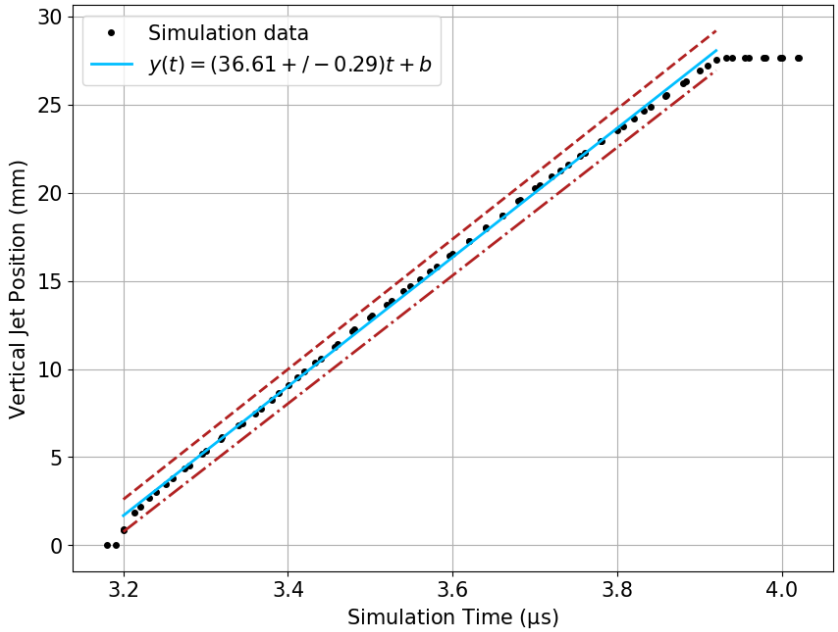

Figure 3-6: Vertical jet position versus simulation time (black points) when compressing helium instead of air and a linear fit of the data (solid light blue) and its upper (dashed red) and lower (dash-dotted red) 95% confidence intervals computed over $[3.20, 3.92]$ μs.

3.3 Mesh Convergence

We conducted a mesh convergence study in the case of fixed KBC in order to understand the dependence of jet velocity on mesh resolution. Results from the study are summarized in Table 3-1. It is observed that jet velocity increases with resolution and appears not to converge even at model 5's high resolution.

However, models 4 and 5 resulted in small, dense masses from the steel piston accelerating to lead the jet along the axisymmetric boundary. This is an important qualitative difference between models 1—3 and 4—5 and is responsible for the velocities reported. Without this effect, the jet velocities of models 4 and 5 would certainly be slower.

Table 3-1: Results from a mesh convergence study.

Model	$dx_{\min}$	$dx_{\max}$	Jet Vel.	Fit Interval
—	(μm)	(μm)	(km/s)	(μs)
1	50.80	406.4	10.17 ± 0.11	[4.12, 5.00]
2	25.40	203.2	11.96 ± 0.055	[4.12, 4.80]
3	12.70	101.6	13.46 ± 0.060	[4.12, 4.84]
4*	6.350	50.80	20.96 ± 0.21	[4.12, 4.66]
5*	3.175	25.40	30.14 ± 0.059	[4.12, 4.15]

Additionally, and perhaps as an explanation for the qualitative differences observed in models 4 and 5, we note that fine resolutions such as 12.7 μm may not be consistent with the material models used. Such small scales may be comparable to or smaller than the grain size of materials such as steel, mica, PMMA, and copper making the use of macro scale strength models inappropriate. Therefore, the high resolution results should be considered with additional skepticism.

3.4 Measuring Jet Position

Measuring jet position as the furthest downstream location with a particle velocity greater than 3 km/s would certainly be reasonable if our models did not contain effects such as small, dense masses leading the jet along the axisymmetric boundary. However, such irregularities occur and prompt us to reconsider our velocity metric.

We present one alternative metric here. In addition to requiring a high velocity we take a threshold to consider only zones containing at least 10% STP air[2] by volume and measure the 75^{th} percentile of data in order to track the bulk of the STP air material. By 75^{th} percentile we mean that jet position was taken to be the location within the shock tube for which 75% of zones containing STP air material were upstream and 25% of such zones were downstream. We use this alternative metric to reanalyze models 4 and 5 and show the results in Table 3-2, comparing them to the results obtained using the original metric described in Section 3. For reference, we also include jet velocities for model 3, which was free of the issue of small masses of steel affecting the jet velocity.

Taking the 75^{th} percentile of air artificially decreases the measured jet velocity, but successfully prevents small steel masses accelerating along the axisymmetric boundary from influencing the jet velocity. From model 3 we see that taking the 75^{th} percentile artificially slows the jet by about

[2]By STP air we mean air that was initialized at STP and within the compression chamber.

Table 3-2: Using bulk air location to measure jet velocity.

Model	Metric	Jet Vel.	Fit Interval
—	—	(km/s)	(μs)
3	original	13.46 ± 0.060	[4.12, 4.84]
3	75% air	10.38 ± 0.32	[4.12, 5.00]
4	original	20.96 ± 0.21	[4.12, 4.66]
4	75% air	12.66 ± 0.26	[4.12, 4.95]
5	original	30.14 ± 0.059	[4.12, 4.15]
5	75% air	15.55 ± 0.39	[4.12, 4.16]

30%. Assuming that taking the 75^{th} percentile artificially slows the jets of models 4 and 5 by a similar amount, we can make a crude attempt to "correct" the jet velocities of models 4 and 5 by multiplying by 1.3. Doing so yields 16.46 km/s and 20.22 km/s for models 4 and 5 respectively. Comparing these "corrected" results to Table 3-1 we do not see convergence. Again, we find that jet velocity increases with resolution.

4 Conclusions

Accurately simulating the acceleration of a jet within a Voitenko–like shock tube device is known to be difficult and is important in the context of hypervelocity launcher technology. Here, we presented FLAG hydrocode simulations and discussed their performance.

Our variable resolution model simulated 5 μs using an Eulerian mesh relaxation strategy. The PBX-9407 was simulated to accelerate the steel piston to $\sim$ 5 km/s resulting in a jet velocity of 14.88 km/s and 6.94% error compared to experiment. However, these results were influenced by small masses of steel piston traveling down the shock tube. This effect tended to occur at higher spatial resolutions that may be outside the regime of model applicability for the steel material.

Replacing the physical membrane with a fixed kinetic boundary condition yielded jets with a larger average velocity. Such simulations were used to test the effect of compressing helium rather than air, which was to increase the jet velocity by 270%. Simulations using a kinetic boundary condition were also used in a mesh convergence study, which showed that jet velocity increased with higher spatial resolution.

Because high spatial resolution may be required to achieve large jet velocities but can result in reduced model applicability for materials such as steel, it may be less challenging to accurately model the operation of large scale Voitenko-like shock tube devices rather than miniature devices. For example, the device described by Tasker et al. [29] uses a shock tube bore two orders of magnitude larger in diameter than that used in the experiments of Johnson et al. [7] and should be considered for simulation in subsequent research.

We note that the models presented here were calibrated to a single experiment and were developed using fairly limited information. The models have not undergone any validation processes and should not be used for prediction. However, the models do represent a promising first step toward modeling the acceleration of hypervelocity jets through tubes, gaps, and cracks.

In addition to validation processes an uncertainty quantification assessment of the FLAG models presented here would be useful. There are many uncertainties associated with the experimental setup such as in the axial alignment of the PBX with the PMMA housing, degree of inhomogeneity in the PBX, geometry of the PMMA housing components such as the compression chamber, the initial pressures of the gases, the degree of contamination of the shock tube devices with environmental debris, variation in membrane properties, and other uncertainties not listed here.

We conclude that for certain purposes FLAG may be able to adequately simulate the acceleration of gases in shock tube environments, but that more work is required to be able to robustly simulate such phenomena.

References

[1] C. E. Johnson et al. *Experiments and Modeling of a Miniature Hypervelocity Shock Tube*. Tech. rep. LA-UR-13-28426. Los Alamos National Lab., 2013.

[2] D. Burton. *Connectivity structures and differencing techniques for staggered-grid free-Lagrange hydrodynamics*. Tech. rep. June 1992. URL: https://www.osti.gov/biblio/10161662.

[3] D. Burton. *Multidimensional discretization of conservation laws for unstructured polyhedral grids*. Tech. rep. Aug. 1994. URL: https://www.osti.gov/biblio/35336.

[4] D. Burton. *Consistent finite-volume discretization of hydrodynamic conservation laws for unstructured grids*. Tech. rep. Oct. 1994. URL: https://www.osti.gov/biblio/71618.

[5] James L. Hill. *FLAG user's manual*. Tech. rep. LA-CP-17-20057. Los Alamos National Lab., Jan. 2017.

[6] D. Burton et al. "Compatible, energy conserving, bounds preserving remap of hydrodynamic fields for an extended ALE scheme". In: *Journal of Computational Physics* 355 (2018), pp. 492–533. ISSN: 0021-9991. DOI: https://doi.org/10.1016/j.jcp.2017.11.017.

[7] C. E. Johnson et al. *Experiments on a Miniature Hypervelocity Shock Tube*. Tech. rep. Nov. 2013. URL: https://www.osti.gov/biblio/1098272.

[8] A. E. Voitenko. "Generation of High-Speed Gas Jets". In: *Soviet Physics Doklady* 9 (Apr. 1965), p. 860.

[9] NASA. *Two Stage Light Gas Guns*. https://www.nasa.gov/centers/wstf/site_tour/remote_hypervelocity_test_laboratory/two_stage_light_gas_guns.html. Accessed: 2023-04-10. 2016.

[10] D. Janches et al. "On the geocentric micrometeor velocity distribution". In: *Journal of Geophysical Research: Space Physics* 108.A6 (2003). DOI: https://doi.org/10.1029/2002JA009789.

[11] D. J. Kessler and B. G. Cour-Palais. "Collision frequency of artificial satellites: The creation of a debris belt". In: *Journal of Geophysical Research: Space Physics* 83.A6 (1978), pp. 2637–2646. DOI: https://doi.org/10.1029/JA083iA06p02637.

[12] M. Crawford. *New Nanomaterial Proves Stronger Than Kevlar*. https://www.asme.org/topics-resources/content/new-nanomaterial-proves-stronger-than-kevlar?utm_source=ME&utm_medium=email&utm_campaign=03272023_ME_Newsletter&utm_content=SEG0022583&asmepromo=MER0028651. Accessed: 2023-05-09. 2023.

[13] J. Huneault et al. "An explosively driven launcher capable of 10kms^{-1} projectile velocities." In: *Shock Waves* 32 (2022), pp. 569–591. DOI: https://doi.org/10.1007/s00193-022-01095-1.

[14] C. R. Noble et al. *ALE3D: An Arbitrary Lagrangian-Eulerian Multi-Physics Code*. Tech. rep. LLNL-TR-732040. Lawrence Livermore National Lab., May 2017. DOI: 10.2172/1361589. URL: https://www.osti.gov/biblio/1361589.

[15] D. Burton. *Consistent finite-volume discretization of hydrodynamic conservation laws for unstructured grids*. Tech. rep. UCRL-JC-118788. Lawrence Livermore National Lab., Oct. 1994.

[16] S. P. Lyon and J. D. Johnson. *SESAME: The Los Alamos National Laboratory Equation of State Database*. Tech. rep. LA-UR-92-3407. Los Alamos National Lab., Oct. 1992.

References

[17] J. A. Bearden. "A Precision Determination of the Viscosity of Air". In: *Phys. Rev.* 56 (10 Nov. 1939), pp. 1023–1040. DOI: 10.1103/PhysRev.56.1023. URL: https://link.aps.org/doi/10.1103/PhysRev.56.1023.

[18] O. Reynolds. "XXIX. An experimental investigation of the circumstances which determine whether the motion of water shall be direct or sinuous, and of the law of resistance in parallel channels". In: *Philosophical Transactions of the Royal society of London* 174 (1883), pp. 935–982.

[19] H. Schlichting and K. Gersten. "Onset of Turbulence (Stability Theory)". In: *Boundary-Layer Theory*. Berlin, Heidelberg: Springer Berlin Heidelberg, 2017, pp. 415–496. ISBN: 978-3-662-52919-5. DOI: 10.1007/978-3-662-52919-5_15.

[20] W. Bo and M. Shashkov. "Adaptive reconnection-based arbitrary Lagrangian Eulerian method". In: *Journal of Computational Physics* 299 (2015), pp. 902–939. ISSN: 0021-9991. DOI: https://doi.org/10.1016/j.jcp.2015.07.032.

[21] J. N. Plohr. *Preston-Tonks-Wallace (PTW) Visco-Plasticity Model*. Tech. rep. Los Alamos National Lab., Sept. 2018. DOI: 10.2172/1469503. URL: https://www.osti.gov/biblio/1469503.

[22] J. N. Plohr. *The Preston-Tonks-Wallace (PTW) Model Parameterization of Stainless Steel 304L: Comparison between Annealed and As-Received Specimens*. Tech. rep. LA-UR-18-24395. Los Alamos National Lab., May 2018.

[23] D. J. Steinberg. *Equation of State and Strength Properties of Selected Materials*. Tech. rep. UCRL-MA-106439. Lawrence Livermore National Lab., Feb. 1996.

[24] S&R Optic GmbH. *Properties of Mica*. https://www.sr-optic.com/Materials/Mica/. Accessed: 2023-04-05. 2022.

[25] D. Mandell, D. Burton, and C. Lund. *High explosive programmed burn in the FLAG code*. Tech. rep. Feb. 1998. DOI: 10.2172/572664. URL: https://www.osti.gov/biblio/572664.

[26] M. A. Kenamond. *Lund high explosive programmed burn model in FLAG code*. Tech. rep. LA-UR-09-08297. Los Alamos National Lab., Dec. 2009.

[27] R. Menikoff. *JWL Equation of State*. Tech. rep. Los Alamos National Lab., Dec. 2015. DOI: 10.2172/1229709. URL: https://www.osti.gov/biblio/1229709.

[28] B. M. Dobratz. *LLNL explosives handbook: properties of chemical explosives and explosives and explosive simulants*. Tech. rep. Lawrence Livermore National Lab., Mar. 1981. DOI: 10.2172/6530310. URL: https://www.osti.gov/biblio/6530310.

[29] D. G. Tasker et al. "Voitenko experiments with novel diagnostics detect velocities of 89 km/s". In: *International Journal of Impact Engineering* 135 (2020), p. 103406.